View metadata, citation and similar papers at core.ac.uk

brought to you by CORE

provided by Universidad Carlos III de Madrid e-Archivo

This is a postprint version of the following published document:

Pastor-Rodríguez, A., Sánchez-Arriaga, G., Sanjurjo-Rivo, M. (2017). Modeling and Stability Analysis of Tethered Kites at High Altitudes. *Journal of Guidance, Control, and Dynamics*, 40(8), pp.: 1892-1901.

DOI: https://doi.org/10.2514/1.G002550

© 2017 by the American Institute of Aeronautics and Astronautics, Inc. All rights reserved. All requests for copying and permission to reprint should be submitted to CCC at www.copyright.com; employ the ISSN 0731-5090 (print) or 1533-3884 (online) to initiate your request. See also AIAA Rights and Permissions www.aiaa.org/randp.

Modeling and stability analysis of tethered kites at high-altitudes

A. Pastor-Rodríguez*, G. Sánchez-Arriaga†, and M. Sanjurjo-Rivo‡
Bioengineering and Aerospace Engineering Department,
Universidad Carlos III de Madrid, 28911, Spain

A systematic analysis of the role played by several physical mechanisms in the longitudinal stability of a tethered kite is presented. A simple model, which artificially constrains the pitch motion of the kite and approximates the tether by a massless and rigid bar, is improved progressively to include the kite pitch motion as well as tether inertia, flexibility, wind load and elasticity. The models are presented as compact sets of ordinary differential equations without algebraic constraints, which are explicitly eliminated by making an extensive use of Lagrangian mechanics. The contributions of each physical mechanism on kite stability is investigated separately and a trade-off between the complexity and computational costs of the models against their accuracy and reliability is carried out. The wind load on the tether is identified as a key effect stabilizing the steady state of kites. Optimal bridle design and tether length selection to compute the kite ceiling is discussed.

Nomenclature

AR	= kite aspect ratio
b	= kite span, m
c	= kite chord, m
C_L	= kite lift coefficient
C_D	= kite drag coefficient
$C_\perp$	= tether normal aerodynamic coefficient
d_t	= tether diameter, m
f_t	= tether damping coefficient,
g	= gravitational acceleration, m/s^2
I_k	= kite moment of inertia, kgm^2
L_B	= bridle length, m
L_t	= unstretched tether length, m
m_k	= kite mass, kg
ρ	= air density, kg/m^3
$\mathbf{R}_i$	= bar i position vector, m
$\mathbf{R}_k$	= kite position vector, m
S	= kite surface, m^2
$\mathbf{T}$	= tether tension, N
$\mathbf{V}_i$	= bar i velocity, m/s
$\mathbf{V}_w$	= wind speed, m/s
$\mathbf{V}_k$	= kite velocity, m/s
$\boldsymbol{F}_A$	= Aerodynamic force, N
$\boldsymbol{M}_A$	= Aerodynamic torque, Nm
α	= kite angle of attack, rad
δ	= bridle angle, rad
Γ_i	= bar i elevation angle, rad
$\boldsymbol{\Omega}_i$	= bar i angular velocity, rad/s
$\boldsymbol{\Omega}_k$	= kite angular velocity, rad/s
θ	= kite pitch angle, rad

*M. S. Student, Bioengineering and Aerospace Engineering Department, Universidad Carlos III de Madrid, 28911, Leganés, Spain
†Ramón y Cajal Research Fellow, Bioengineering and Aerospace Engineering Department, Universidad Carlos III de Madrid, 28911, Leganés, Spain
‡Visiting Professor, Bioengineering and Aerospace Engineering Department, Universidad Carlos III de Madrid, 28911, Leganés, Spain

I. INTRODUCTION

Flying bodies linked to the ground by tethers, including kites and balloons, have a wide range of applications like high-altitude wind power generation[1–4], aerial photography[5], and sport activities like kite surfing among others. For all of them, good stability characteristics of the steady state are desirable and, for this reason, stabilization elements, as tails, lateral areas, longitudinal dihedral, or a fine tune of the bridle, are used. However, they often reduce kite performance. The identification of the physical mechanisms responsible for the unstable behaviour is a difficult task due to the complex interplay of structural and aerodynamic effects that are superimposed to the natural fluctuations of the wind velocity. A thorough investigation of dynamical models with disparate complexity can help in separating the different contributions and identifying the dominant instability mechanisms. This sequential stepping will provide a deep understanding of the kite dynamics and it can help in the development of efficient, reliable and robust kite flight simulators.

Several kite models has been presented already in the literature. Concerning the kite itself, flexibility effects are normally ignored. There are yet some exceptions, which implemented multibody reduction approach techniques [6], lumped masses [7] or aeroelastic model embedded in the dynamic equation [8]. Regarding the tether, many different approximations exist. The simplest analysis substituted the tether by a rigid and massless bar [9][10][11]. More refined models for inelastic [12, 13] and elastic [7, 14] tethers considered lumped masses joined by bars or springs, respectively. Trustworthy tether models have also been developed by the space tether community. Some of them are based on finite-element algorithms for elastic tethers [15], others used Minakov's theory [16], and two-bar [17] and N-bar [18, 19] models for inelastic tethers. The latter inspired the novel kite-tether model with an arbitrary number of bars that is presented in this work.

In many important kite applications, like airborne

wind turbines, kite aerial photography and breaking the kite altitude world record, the equilibrium of the symmetric steady state of the tether-kite system is crucial. Typically kites are designed for these applications with a high lateral-directional stability and the motion is mainly restricted to a vertical plane that coincides with the plane of symmetry of the kite. Within this framework, a longitudinal analysis of the kite dynamics is fully justified. A rigid body approximation for the kite is also valid if the study is focused on small perturbations close to the equilibrium. Both hypothesis are taken hereafter.

This work presents a systematic analysis of the role played by several physical mechanisms in the longitudinal stability of a kite. It starts with a model that ignores the pitch motion of the kite as well as tether inertia, flexibility, air drag and elasticity. All these effects are incorporated one by one to the model. A trade-off of the raising of the complexity, computational cost, accuracy and reliability of the mathematical models is carried out. In order to compare these features, the steady states of the tether-kite system and their linear stability are investigated. Following previous works on kite dynamics [10, 20–22], we made an extensive use of Lagrangian formulation and implemented a *minimal coordinate approach*. This strategy eliminates explicitly the tether tension and yields a set of ordinary differential equations. It differs from a *natural coordinate approach*, which leads to a nonlinear system of mixed ordinary and algebraic equations [23]. The body of the article summarizes the key steps to develop the models whereas mathematical details are explained in Appendixes A-C.

II. BASIC AND COMMON FEATURES OF THE KITE MODELS

There is a set of basic features shared by all the models of this work. Since the analysis is restricted to longitudinal motions of the tether-kite system, the dynamics happens in the vertical plane that contains the wind velocity vector $\boldsymbol{V}_w = -V_w \boldsymbol{i}_E$ and the attachment point O_E of the tether with the ground. This plane, spanned by the unit vectors $\boldsymbol{i}_E$ and $\boldsymbol{k}_E$ of an inertial frame of reference, coincides with the plane of symmetry of the kite (see Fig. 1). The analysis also uses a non-inertial frame of reference attached to the kite, with origin at its center of mass G, $\boldsymbol{j}_B = \boldsymbol{j}_E$, and unit vectors $\boldsymbol{i}_B$ and $\boldsymbol{k}_B$ along the principal axes of inertia of the kite.

The most complex of our tether models is characterized by the tether unstretched length L_t, mass m_t, diameter d_t, normal drag coefficient $C_\perp$, Young modulus E_t and damping coefficient f_t. Regarding the kite, it is taken as a rigid body of mass m_k, surface S, chord c, span b, and moment of inertia about $\boldsymbol{j}_B$ equal to I_K. For simplicity, we assumed that the kite is a very thin airfoil of rectangular shape, thus having $S = b \times c$, $I_k = m_k c^2/12$ and its center of mass G at the middle of the rectangle. The kite has a bridle made of two very thin lines of negligible mass that meet at the attachment point Q with the main tether. As we will see, the geometry of the bridle, here characterized by the distance L_B between G and Q and angle δ ($\overline{GQ}/L_B = \cos\delta \boldsymbol{i}_B + \sin\delta \boldsymbol{k}_B$), plays a central role in kite stability and performance (see inset in Fig. 1). The models assume that the kite and the bridle move as a rigid body.

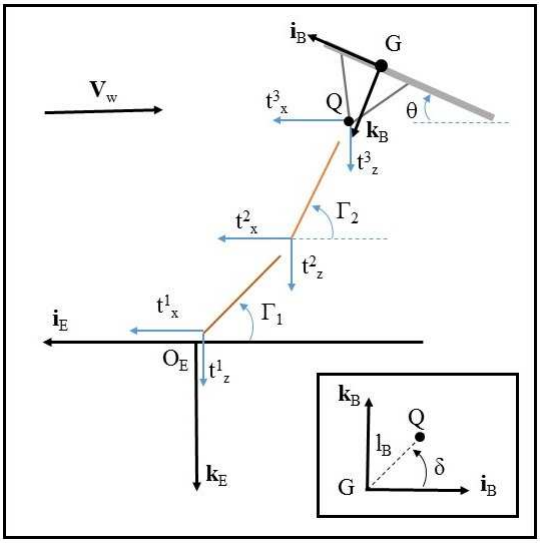

FIG. 1: Frame of references, coordinates and bridle geometry (inset).

In order to identify the key parameters that control kite dynamics, the equations of motions are written in dimensionless form. The characteristic magnitudes of the analysis are: kite mass m_k, the unstretched tether length L_t and the gravitational acceleration g. Dimensionless variables are denoted by lower case letters whereas capital letters correspond to variables with dimensions. In this way, the position vector and velocity of the center of mass of the kite are $\boldsymbol{R}_k = L_t \boldsymbol{r}_k$, $\boldsymbol{V}_k = \sqrt{gL_t}\boldsymbol{v}_k$; the aerodynamic force and moment about the center of mass are $\boldsymbol{F}_A = m_k g \boldsymbol{f}_A$, $\boldsymbol{M}_A = m_k g L_t \boldsymbol{m}_A$; and the moment of inertia of the kite is $I_k = m_k L_t^2 i_k$. Derivatives with respect to the dimensionless time $\tau = \sqrt{g/L_t}t$ are denoted with with dots. Euler-Lagrange equations then read

$$\frac{\mathrm{d}}{\mathrm{d}\tau}\left(\frac{\partial \mathcal{L}}{\partial \dot{x}_{si}}\right) - \frac{\partial \mathcal{L}}{\partial x_{si}} = Q_i \tag{1}$$

with $\mathcal{L}$ and Q_i the normalized Lagrangian function and generalized forces and x_{si} the components of the state vector $\boldsymbol{x}_s$ of the kite-tether system (see below).

All the tether-kite descriptions made use of the same aerodynamic model. Concerning the kite, the aerodynamic center is at a distance $c/4$ from the leading edge. In additional, the aerodynamic moment about the aerodynamic center vanishes because the thin airfoil is taken as symmetric. The normalized aerodynamic force and moment about the center of mass produced by lift and

drag are

$$\boldsymbol{f}_{Ak} = -\mu v_A^2 \left[(C_D \cos\alpha - C_L \sin\alpha)\, \boldsymbol{i}_B + (C_D \sin\alpha + C_L \cos\alpha)\, \boldsymbol{k}_B \right] \quad (2)$$

$$\boldsymbol{m}_{Ak} = \mu v_A^2 \frac{\epsilon_c}{4} (C_D \sin\alpha + C_L \cos\alpha)\, \boldsymbol{j}_B \quad (3)$$

where $\mu \equiv \rho S L_t / 2m_k$, $\epsilon_c = c/L_t$ and ρ is the air density, $\boldsymbol{v}_{Ak} = \boldsymbol{v}_k - \boldsymbol{v}_w$ is the normalized aerodynamic velocity of the kite and its angle of attack is given by

$$\alpha = \arctan\left(\frac{\boldsymbol{v}_{Ak} \cdot \boldsymbol{k}_B}{\boldsymbol{v}_{Ak} \cdot \boldsymbol{i}_B} \right) \quad (4)$$

The lift and drag coefficients of the kite in Eqs. 2-3 follow the simple relations

$$C_L(\alpha) = \frac{\pi}{2} AR\alpha, \qquad C_D(\alpha) = C_{D0} + \frac{2}{\pi AR} C_L^2 \quad (5)$$

where $AR = b^2/S$ is the aspect ratio and C_{D0} the zero-lift drag coefficient. This linear model in α for C_L is valid up to the stall angle α_s. This range of validity is taken into account when the results of this work are presented.

Regarding the tether, we followed Refs. [25] and [26] and decomposed the aerodynamic force into a component normal to the tether and one tangential to it (instead of the usual decomposition into drag and lift used in other works [27–29]). Since the normal and tangential aerodynamic coefficient for a round tether satisfy $C_\perp >> C_\parallel$, we will ignore the aerodynamic force component tangent to the tether. The normalized aerodynamic force on a differential element of length $\mathrm{d}l_t$ then reads

$$\mathrm{d}\boldsymbol{f}_{At} = \chi \left(\boldsymbol{v}_A \cdot \boldsymbol{u}_\perp \right)^2 \boldsymbol{u}_\perp \mathrm{d}l_t \quad (6)$$

with $\chi \equiv C_\perp/2 \times \rho L_t^2 d_t / m_k$, v_A is the normalized aerodynamic velocity component of the tether element and $\boldsymbol{u}_\perp$ the unit vector normal to the tether satisfying $\boldsymbol{v}_A \cdot \boldsymbol{u}_\perp < 0$. Table I summarizes the value of the parameters used in this work.

Symbol	Value	Symbol	Value
g	9.81 m/s^2	ρ	1.225 kg/m^3
b	3 m	c	1.5 m
L_t	100 m	L_B	0.5 m
m_k	2.0 kg	C_{D0}	0.005
α_s	25°	ρ_t	$970 kg/m^3$
$C_\perp$	1	d_t	$3mm$
E_t	$90GPa$	f_t	0.1

TABLE I: Kite and tether parameters.

Equation 1 is a set of second order ordinary differential equations that, after introducing the vector $\boldsymbol{u} = [\boldsymbol{x}_s \;\; \dot{\boldsymbol{x}}_s]$, takes the form

$$\frac{\mathrm{d}\boldsymbol{u}}{\mathrm{d}\tau} = \boldsymbol{h}(\boldsymbol{u}) \quad (7)$$

These equations describe the non-linear dynamics of the kite-tether system and can be applied to the analysis of any type of orbits and their stability. From the point of view of airborne wind energy generation, one of the most interesting case corresponds to periodic orbits, which has been investigated using other models in the past (see for instance [30] and references therein). In this work, we will investigate the equilibrium states $\boldsymbol{u}^* = [\boldsymbol{x}_s^* \;\; \boldsymbol{0}]$ of the system. These states satisfy the condition

$$\boldsymbol{h}(\boldsymbol{u}^*) = 0 \quad (8)$$

The stability of $\boldsymbol{u}^*$ is studied by adding a small perturbation of the form $\boldsymbol{u}(\tau) = \boldsymbol{u}^* + \boldsymbol{u}^1(\tau)$ and substituting in Eq. 7

$$\frac{\mathrm{d}\boldsymbol{u}^1}{\mathrm{d}\tau} = \boldsymbol{J}\,|_{\boldsymbol{u}^*}\, \boldsymbol{u}^1 + O(|\boldsymbol{u}^1|^2) \quad (9)$$

The Jacobian $\boldsymbol{J}\,|_{\boldsymbol{u}^*}$ of the flux $\boldsymbol{h}(\boldsymbol{u})$ plays a central role in the stability analysis. The equilibrium $\boldsymbol{u}^*$ is asymptotically stable if all the eigenvalues λ_j of $\boldsymbol{J}\,|_{\boldsymbol{u}^*}$ have negative real parts. The eigenvectors gives us information about the basic kite-tether motions close to the equilibrium (eigenmodes).

III. BAR-BASED MODELS TO SIMULATE INELASTIC TETHERS

One of the major issues when modelling tethers is the stiffness of the resulting set of equations, which is caused by the drastic difference between the longitudinal and lateral wave velocities ($\sqrt{E_t/\lambda_t} >> \sqrt{T/\lambda_t}$ with λ_t and T the linear tether density and tension). However, the natural dissipation by internal friction of longitudinal waves happens more quickly than for transverse waves. Moreover, in many kite applications the tension is not high enough to produce significant deformation of the tether and an inelastic tether model is adequate. This choice is advantageous because the fast longitudinal oscillations along the tether are automatically eliminated and the resulting set of differential equations is not stiff. Here we develop a robust and efficient model to simulate a kite linked to the ground by an inelastic tether. The Lagrangian formulation eliminates from the equations of motion the tether tension, which can be computed in a post-process of the result of the simulation (see a detailed explanation in Appendix B).

The inelastic tether is substituted by N rigid bars of length L_t/N, mass m_t/N, and moment of inertia about the center of mass $m_t L_t^2/(12N^3)$. The bars are connected by ideal joints with no dissipation. Figure 1 shows a diagram of a kite-tether system using just a couple of bars, where the joints between the first bar and the origin, adjacent bars, and the bar N and the kite were separated for clarity. The system has $N+1$ degrees of freedom that we gather in the state vector

$$\boldsymbol{x}_s = [\Gamma_1 \;\; \Gamma_2 \;\; ... \;\; \Gamma_N \;\; \theta] \quad (10)$$

In order to find the Lagrangian of the system we carried out some kinematic calculations. The (dimensionless) angular velocity and vector position and velocity of the center of mass of the bar named i are given by

$$\boldsymbol{\omega}_i = -\dot{\Gamma}_i \boldsymbol{j}_E \tag{11}$$

$$\boldsymbol{r}_i = -\frac{1}{N}\sum_{j=1}^{i} p_j \left(\cos\Gamma_j \boldsymbol{i}_E + \sin\Gamma_j \boldsymbol{k}_E\right) \tag{12}$$

$$\boldsymbol{v}_i = \frac{1}{N}\sum_{j=1}^{i} p_j \dot{\Gamma}_j \left(\sin\Gamma_j \boldsymbol{i}_E - \cos\Gamma_j \boldsymbol{k}_E\right) \tag{13}$$

The factors p_j, which always appear inside a sum, take the value

$$p_j = \begin{cases} 1 & j < i \\ 1/2 & j = i \end{cases} \tag{14}$$

with i the maximum index of the summation. For instance, in the equations above, $p_j = 1$ for $j < i$ and $p_j = 1/2$ for $j = i$. Similar kinematic calculations for the kite are

$$\boldsymbol{\omega}_k = \dot{\theta} \boldsymbol{j}_E \tag{15}$$

$$\boldsymbol{r}_k = -\frac{1}{N}\sum_{j=1}^{N} \left(\cos\Gamma_j \boldsymbol{i}_E + \sin\Gamma_j \boldsymbol{k}_E\right) - l_B \left[\cos\left(\delta - \theta\right) \boldsymbol{i}_E + \sin\left(\delta - \theta\right) \boldsymbol{k}_E\right] \tag{16}$$

$$\boldsymbol{v}_k = \frac{1}{N}\sum_{j=1}^{N} \dot{\Gamma}_j \left(\sin\Gamma_j \boldsymbol{i}_E - \cos\Gamma_j \boldsymbol{k}_E\right) - l_B \dot{\theta} \left[\sin\left(\delta - \theta\right) \boldsymbol{i}_E - \cos\left(\delta - \theta\right) \boldsymbol{k}_E\right] \tag{17}$$

From Eqs. 11-17 one finds the normalized Lagrangian function

$$\mathcal{L}\left(\boldsymbol{x}_s, \dot{\boldsymbol{x}}_s\right) = \frac{1}{2}\left(v_k^2 + i_k \omega_k^2\right) + \boldsymbol{r}_k \cdot \boldsymbol{k}_E \frac{\sigma}{2}\sum_{j=1}^{N}\left(\frac{v_j^2}{N} + i_e \omega_j^2\right) + \frac{\sigma}{N}\sum_{j=1}^{N} \boldsymbol{r}_j \cdot \boldsymbol{k}_E, \tag{18}$$

which is the difference between the kinetic and potential energy of the system. In Eq. 18 we introduced the parameters $\sigma \equiv m_t/m_k$ and $i_e = 1/(12N^3)$. The generalized forces in Eq. 1 are given by

$$Q_{\Gamma_i} = \boldsymbol{f}_{Ak} \cdot \frac{\partial \boldsymbol{v}_k}{\partial \dot{\Gamma}_i} + \sum_{j=1}^{N} \boldsymbol{f}_{At}^j \cdot \frac{\partial \boldsymbol{v}_j}{\partial \dot{\Gamma}_i} \tag{19}$$

$$Q_\theta = \boldsymbol{f}_{Ak} \cdot \frac{\partial \boldsymbol{v}_k}{\partial \dot{\theta}} + \boldsymbol{m}_{Ak} \cdot \frac{\partial \boldsymbol{\omega}_k}{\partial \dot{\theta}} \tag{20}$$

where we took into account that $\partial \boldsymbol{v}_j/\partial\dot{\theta} = \partial \boldsymbol{\omega}_j/\partial\dot{\theta} = \partial \boldsymbol{\omega}_k/\partial\dot{\Gamma}_i = 0$ and assumed that the aerodynamic moment on each bar is negligible. The total aerodynamic force at bar j, named $\boldsymbol{f}_{At}^j$, is computed from Eq. 6. We ignore the aerodynamic velocity variations along a bar and write

$$\boldsymbol{f}_{At}^j = \frac{\chi}{N}\left(\boldsymbol{v}_A^j \cdot \boldsymbol{u}_\perp^j\right)^2 \boldsymbol{u}_\perp^j \tag{21}$$

with $\boldsymbol{v}_A^j = \boldsymbol{v}_j - \boldsymbol{v}_w$ and $\boldsymbol{u}_\perp^j = \pm\left(\sin\Gamma_j \boldsymbol{i}_E - \cos\Gamma_j \boldsymbol{k}_E\right)$ (the sign should be chosen to have $\boldsymbol{v}_{Aj} \cdot \boldsymbol{u}_\perp^j < 0$). It is remarkable that tether tension, which is an ideal (workless) holonomic constraint force, does not appear in Eqs. 19 and 20.

The explicit form of Eqs. 18, 19 and 20 as a function of $\boldsymbol{x}_s$ and $\dot{\boldsymbol{x}}_s$ are given in Appendix A.

A. Massless one-bar model with constrained kite pitch motion

The simplest kite model is obtained by taking just one bar ($N = 1$) without inertia ($\sigma = 0$) and tether aerodynamic force ($\chi = 0$), and forcing the kite pitch angle to follow the law

$$\theta(\tau) = \frac{\pi}{2} - \Gamma(\tau) \tag{22}$$

This same model was used in the past, but with a slightly different formulae for C_L and C_D, to investigate the kite equilibrium and the existence of a Hopf bifurcation and longitudinal periodic orbits [9]. In this case, we find from Eq. A1 a very simple form for the Lagrangian

$$\mathcal{L}(\Gamma, \dot{\Gamma}) = \kappa\frac{\dot{\Gamma}^2}{2} - \sin\Gamma + l\cos\left(\Gamma + \delta\right) \tag{23}$$

with $\kappa \equiv \left(1 + l_B^2 + 2l_B\sin\delta + i_k\right)$. The equation of motion of the only degree of freedom of the model, i.e. the elevation angle of the bar Γ, takes the form (see Eq. A3)

$$\kappa\ddot{\Gamma} + \cos\Gamma + l_B\sin\left(\Gamma + \delta\right) = -\boldsymbol{m}_{Ak} \cdot \boldsymbol{j}_B + \left(1 + l_B\sin\delta\right)\boldsymbol{f}_{Ak} \cdot \boldsymbol{i}_B - l_B\cos\delta \boldsymbol{f}_{Ak} \cdot \boldsymbol{k}_B \tag{24}$$

The equilibrium elevation angle of the tether, Γ^*, is found by setting $\ddot{\Gamma} = \dot{\Gamma} = 0$ in Eq. 24 and solving the non-linear algebraic equation

$$\cos\Gamma^* + l_B\sin\left(\Gamma^* + \delta\right) = \mu v_w^2 \left\{C_L\left[\cos\Gamma^* - \frac{\epsilon_c}{4}\sin\Gamma^* + l_B\sin(\delta + \Gamma^*)\right] - C_D\left[\sin\Gamma^* + \frac{\epsilon_c}{4}\cos\Gamma^* - l_B\cos(\delta + \Gamma^*)\right]\right\} \tag{25}$$

where we used that, at the kite equilibrium, $v_A = v_w$ and $\alpha^* = \theta^* = \pi/2 - \Gamma^*$. Panel (a) in Fig. 2 shows the tether elevation angle Γ^* given by Eq. 25 versus the wind velocity for three values of the bridle angle δ. The influence of δ for this model is very weak and the three lines almost overlap. Since the aerodynamic force should balance the weight of the kite, the angle of attack increases (and the elevation angle decreases following the constraint $\alpha^* = \pi/2 - \Gamma^*$) as the wind velocity decreases.

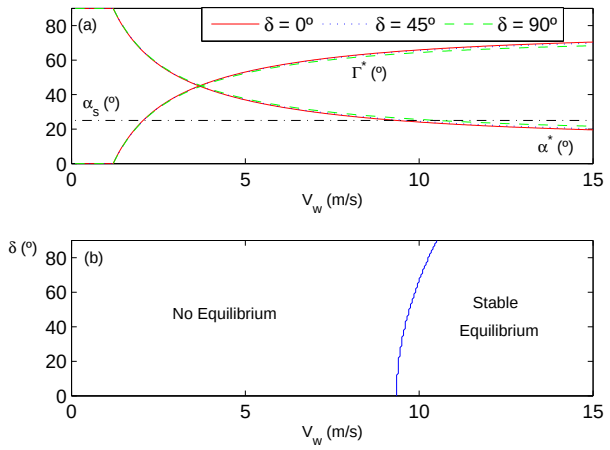

FIG. 2: Equilibrium of a massless one-bar kite model with constrained pitch angle.

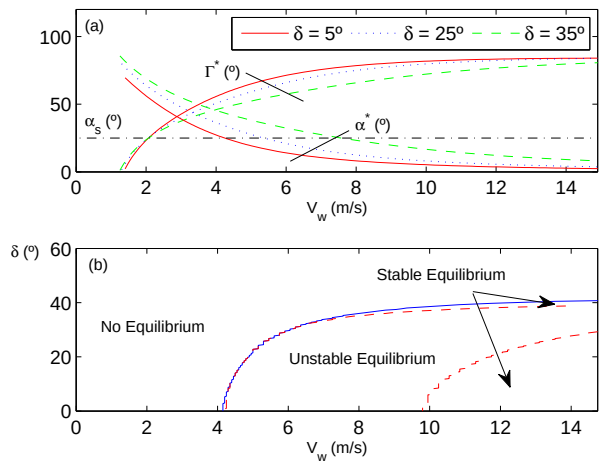

FIG. 3: Equilibrium of a 1-bar kite model without tether inertia.

For each value of δ, there is a minimum wind velocity that makes the steady kite flight possible with attack angle below the stall [see Panel (b)]. As δ increases, the required wind is higher.

The linear stability analysis shows that the equilibrium state $\boldsymbol{u}^* = [\Gamma^* \;\; 0]$ is stable within the parametric domain shown in Fig. 2. The matrix $\boldsymbol{J}\,|_{\boldsymbol{u}^*}$ has a pair of complex conjugated eigenvalues with negative real part. For this model, which has 1 degree of freedom, the tether and the kite move as a rigid solid similar to an inverted pendulum.

B. One-bar model

We now investigate the role played by the kite pitch attitude by removing the constraint $\theta = \pi/2 - \Gamma$. The system has two degrees of freedom, being the state vector $\boldsymbol{x}_s = [\Gamma \;\; \theta]$. The lagrangian of the system is found from Eq. A1 with $N = 1$. It reads

$$\mathcal{L}\left(\boldsymbol{u}, \dot{\boldsymbol{u}}\right) = \frac{1}{2}\left[1 + \sigma\left(i_e + \frac{1}{4}\right)\right]\dot{\Gamma}^2 + \frac{1}{2}\left(l_B^2 + i_k\right)\dot{\theta}^2 - l_B\dot{\Gamma}\dot{\theta}\cos\gamma - \left(1 + \frac{\sigma}{2}\right)\sin\Gamma - l_B\sin\left(\delta - \theta\right) \tag{26}$$

where γ is defined in Eq. A2. If tether inertial effects are ignored, i.e. $\sigma = 0$, Eq. 26 coincides with the Lagrangian function used in Ref. [10]. The equations of motion that govern Γ and θ are obtained by setting $N = 1$ in Eqs. A3 and A4.

For simplicity we first analyze the equilibrium of a kite joined to the ground by a massless ($\sigma = 0$) and infinitely thin ($\chi = 0$) tether. Figure 3 summarizes the main results. A comparison with the results found in Sec. III A shows that letting the kite adopt its own pitch attitude is essential and the artificial constraint $\theta = \pi/2 - \Gamma$ is not realistic. In first place, Panel (b) in Fig. 3 shows that kite equilibrium is not possible if the bridle angle δ is above 40°. In second place, steady flight is possible for much lower wind velocities. For instance, in the model of Sec. III A the minimum wind velocity to fly with attack angle below the stall was about $9,35m/s$. However, only $4m/s$ are needed if the kite pitch angle is taken as a degree of freedom.

An analysis of the eigenvalues and eigenvectors of $\boldsymbol{J}\,|_{\boldsymbol{u}^*}$ reveals that there are two complex eigenmodes: a *pendular mode* that involves tether and kite motions and a *short period mode* that mainly consists on fast oscillations of the kite about point Q [10, 21]. Panel (b) in Fig. 3 shows that kite equilibrium can be unstable for certain combinations of wind velocities and δ values. This feature is missed by the model of Sec. III A. The instability region splits the $\delta - V_w$ plane into two disconnected regions where the equilibrium is stable. Among the two eigenmodes of this 2-degree of freedom model, it is the *pendular mode* that loses stability through supercritical Hopf bifurcations. Inside the instability region enclosed by the dashed line in Panel (b) of Fig. 3, a family of stable periodic orbits exists.

Tether inertia and aerodynamic force affect on the stability domains are shown in Fig. 3 differently. Panel (a) in Fig. 4 shows the stability regions of the kite equilibrium state when tether inertial effects are included ($\sigma \equiv m_t/m_k = 0.34$ according to Table I) but tether aerodynamic force is ignored. A comparison with the bottom panel of Fig. 3 shows that, for this moderate tether-to-kite mass ratio, the parametric domain with unstable equilibria is slightly smaller. Therefore, tether inertia has a stabilizing effect on the longitudinal motion of the kite. The effect of the aerodynamic force on the tether is more dramatic because the instability regions is severely reduced (see panel (b) in Fig. 4). Even for

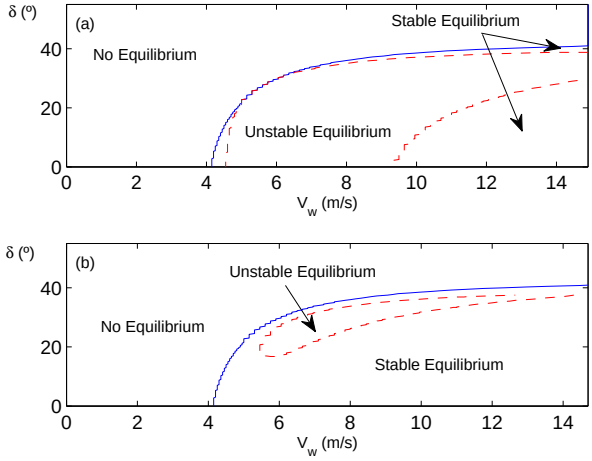

FIG. 4: Equilibrium of a 1-bar kite model with $\chi = 0$ (a) and $\chi \neq 0$ (b).

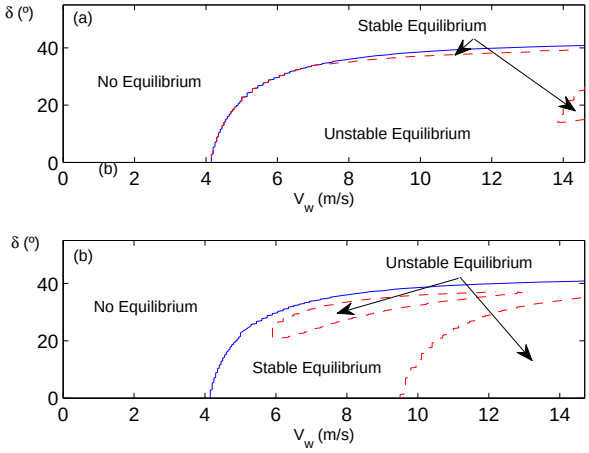

FIG. 5: Equilibrium of a N-bar kite model with $\chi = 0$ (a) and $\chi \neq 0$ (b).

this relatively short tether ($L_t = 100m$) the aerodynamic force plays an important role stabilizing the system.

C. N-bar model

Tether flexibility effects are investigated by setting $N > 1$. As the number of bars used to approximate the tether is increased, new tether oscillations modes appear. Such a rising in the number of degrees of freedom of the system typically makes broader the parametric domain where the steady state is unstable. This statement was verified by computing a stability diagram using Eqs. A3-A4 with $N = 20$ (using $N > 20$ does not change significantly the stability diagram). Panel (a) in Fig. 5 shows the results when the aerodynamic force on the bars is ignored. A comparison with panel (a) of Fig. 3 reveals that flexibility effects can make the kite equilibrium unstable. In agreement with the conclusions of Sec. III B, we also conclude from Panel (b) in Fig. 5 that the aerodynamic force on the tether helps to stabilize the kite-tether system.

Previous analysis indicate that the steady state of the tether-kite system can be unstable in a wide range of conditions. This fact does not necessarily imply that the kite could not fly. For instance, Fig. 6 shows an integration of Eqs. A3-A4 within the range $0 \leq \tau \leq 100$ and with a set of parameters that makes unstable the kite equilibrium ($N = 20$, $\delta = 25°$ and $V_w = 7m/s$, see Panel (b) in Fig. 5). The initial condition was

$$\boldsymbol{u} = \boldsymbol{u}^* + 5 \times 10^{-3} \boldsymbol{v}_1, \tag{27}$$

with $\boldsymbol{v}_1$ the most unstable eigenvector of $\boldsymbol{J}\,|_{\boldsymbol{u}^*}$. Obviously, the orbit moves away from the equilibrium but it converges to a stable periodic orbit. The angle of attack [panel (a)]is always positive and below the stall and

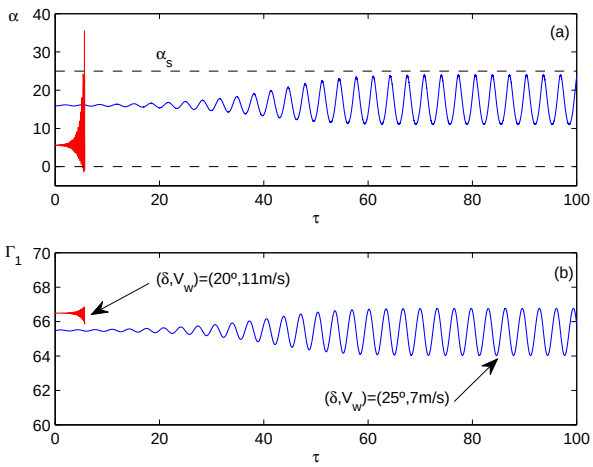

FIG. 6: Attack angle (a) and Γ_1 (b) versus time for two values of v_w and δ.

the amplitude of the oscillations of the first bar is only about 2°. In a real experiment, it would be difficult to distinguish whether the oscillations are self-induced (as predicted by the model) or a consequence of the wind fluctuations. The same computation, but for parameter values within the second unstable domain shown in Fig. 5 ($\delta = 20°$ and $V_w = 11m/s$) reveals that the kite does not always approach to a periodic orbit. As shown in Panel (a) the angle of attack can be negative or above the stall during the transient and our simple aerodynamic model is not trustworthy predicting the kite-tether behavior.

IV. ELASTIC TETHERS

As opposed to the previous bar-based models, a kite linked to the ground by an elastic tether does not present geometric constraints. Therefore, the kite has three degrees of freedom that we gather in the state vector

$$\boldsymbol{x}_s = [\Gamma \quad \theta \quad r] \tag{28}$$

where Γ is, in this section, the angle between $\overline{O_E Q}$ and $-\boldsymbol{i}_E$, $r \equiv |\overline{O_E Q}|/L_t$ and L_t is the unstretched tether length. This set of variables are governed by ordinary differential equations. Their derivation, which is an extension of the models presented in the previous sections, is presented in Sec. C (see Eq. C7).

The state of the elastic tether, which is a continuous medium, is given by the normalized vector position of a tether element $\boldsymbol{r}_t(s,\tau)$ that depends on τ and the unstretched arc-length s of the element. The arc-length covers the range $0 \leq s \leq 1$ and tether tips O_E and Q have $s = 0$ and $s = 1$, respectively. The equation of motion of the tether in normalized form reads

$$\sigma \ddot{\boldsymbol{r}}_t = \boldsymbol{t}' + \sigma \boldsymbol{k}_E + \frac{d\boldsymbol{f}_{At}}{dl} \tag{29}$$

where $d\boldsymbol{f}_{At}/dl$ is given by Eq. 6 and we used a prime to denote partial derivative with respect to the arc-length s. The normalized tether tension is

$$\boldsymbol{t} = \nu\left(\epsilon + f_t \dot{\epsilon}\right) \frac{\boldsymbol{t}'}{\mid \boldsymbol{t}' \mid}, \qquad \nu \equiv \frac{E_t A_t}{m_k g} \tag{30}$$

with $\epsilon = \mid \boldsymbol{t}' \mid -1$, and E_t and A_t the Young's modulus and the cross-section of the tether, respectively. The normal vector in Eq. 6 reads $\boldsymbol{u}_\perp = \pm \boldsymbol{j}_E \times \boldsymbol{r}'/|\boldsymbol{r}'|$ with the sign determined by the condition $\boldsymbol{u}_\perp \cdot \boldsymbol{v}_A < 0$.

The equations of motion of the kite (Eqs. C7) and the tether (Eq. 29) are coupled. Firstly, the generalized forces appearing on the right-hand side of the kite equations involve the tether tension at tip Q (see Eqs. C4-C6). Secondly, the boundary conditions of Eq. 29

$$\boldsymbol{r}_t(0,\tau) = 0, \tag{31}$$

$$\dot{\boldsymbol{r}}_t(0,\tau) = 0, \tag{32}$$

$$\boldsymbol{r}_t(1,\tau) = \boldsymbol{r}_Q \equiv -r\left(\cos\Gamma \boldsymbol{i}_E + \sin\Gamma \boldsymbol{k}_E\right), \tag{33}$$

$$\dot{\boldsymbol{r}}_t(1,\tau) = \boldsymbol{v}_Q \equiv \left(r\dot{\Gamma}\sin\Gamma - \dot{r}\cos\Gamma\right)\boldsymbol{i}_E - \left(\dot{r}\sin\Gamma + r\dot{\Gamma}\cos\Gamma\right)\boldsymbol{k}_E \tag{34}$$

involve the kite variables $\Gamma(\tau)$ and $r(\tau)$. As explained in Appendix C, the partial differential equation for the tether has been discretized with a finite elements method. The state vector of the system (see Eq. C16) includes the degree of freedom of the kite and the positions and the slopes of a given number of points along the tether. After applying the finite element methods, the system is governed by a set of ordinary differential equations similar to Eq. 7.

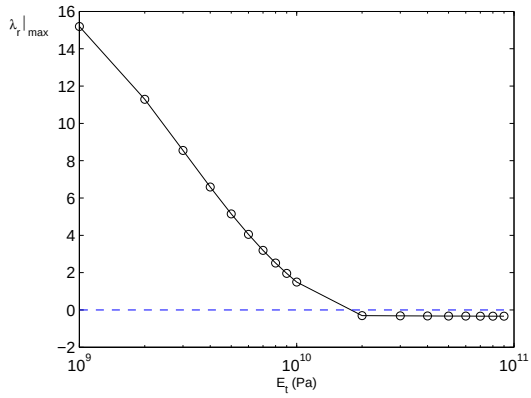

FIG. 7: Maximum of the real part of λ_j versus the Young modulus.

An stability analysis of the steady state of the kite-elastic tether system with 20 finite elements and the parameters of Table I produced almost the same results of the bar-model. We do not show the stability diagram, which is practically equal to Panel (b) in Fig. 5. Therefore, for nominal values of the parameters, the elasticity of the tether does not change the stability. Such a result suggests that a bar-based model is enough to capture correctly the longitudinal dynamics of the kite-tether system. The very different computation cost of both models makes this conclusion relevant.

Nevertheless, a reduction of the Young modulus of the tether can yield different results. For instance, Fig. 7 shows the largest real part among all λ_j of $\boldsymbol{J}\mid_{\boldsymbol{u}^*}$ for the specific values $V_w = 10m/s$ and $\delta = 30°$. For the nominal value $E_t = 90GPa$ this quantity is negative (the equilibrium is stable), in agreement with the explanation of the previous paragraph and Panel (b) in Fig. 5. However, as E_t decreases, the real part of an eigenvalue becomes positive and the steady state is unstable. The appearance of instabilities for low-values of the Young modulus is specially relevant for tether models made of lumped masses connected with springs and dampers. These models are frequently used with unrealistically low values of the springs constant in order to mitigate the stiffness of the differential equations. Therefore, we conclude that such a technique could produce non-physical results and recommend the use of methods, like a bar-based model, that eliminate the fast longitudinal oscillations.

V. KITE CEILING DETERMINATION

In several kite applications the maximum altitude reached by the system is the most important figure of merit. For this reason, we now present a simple procedure to find the optimal kite bridle configuration and tether characteristics that maximize the ceiling. The numerical calculations will use the parameters of Table I,

except for the tether length (L_t), and the bridle parameters (l_B and δ). This section sets the wind velocity to $12m/s$ and uses the N-bar model with $N = 20$.

For a given wind velocity, V_w, the tether length L_t is maximum if the dimensionless velocity $v_w = V_w/\sqrt{L_t g}$ is minimum. Figures 2-5 show that such a condition is met at the boundary that separates the existence regions of the equilibrium, i.e. the angle of attack of the kite is equal to the stall angle, $\alpha = \alpha_s$ and the kite aerodynamic force $\boldsymbol{F}_A$ is maximum. A condition for the minimum tether diameter is then found by assuming $m_k g << |\boldsymbol{F}_A|$ and equating $|\boldsymbol{F}_A|$ with the ultimate load of the tether

$$d_t \mid_{min} = \sqrt{\frac{2\rho S V_w^2}{C_s \pi E_t \sigma_{ul}} \sqrt{C_L^2(\alpha_s) + C_D^2(\alpha_s)}} \tag{35}$$

with σ_{ul} the ultimate tensile strength of the tether and C_s a safety factor. Since the tether aerodynamic force is proportional to d_t, a small tether diameter minimizes the tether bowing and enhances the ceiling.

Using condition $\alpha = \theta^* = \alpha_s$ in Eqs. B5-B7 yields

$$l_B = \frac{\epsilon_c \left(C_D \sin\alpha_s + C_L \cos\alpha_s\right)}{4\left[\left(C_L - \frac{1}{\mu v_w^2}\right)\cos\left(\delta - \alpha_s\right) - C_D \sin\left(\delta - \alpha_s\right)\right]} \tag{36}$$

where the aerodynamic moment and force should be evaluated at $\alpha = \alpha_s$. Therefore, Eq. 36 gives the normalized bridle length l_B, as a function of angle δ, that makes the angle of attack of the kite equal to the stall angle. Panel (a) in Fig. 8 shows the normalized kite altitude versus angle δ for several normalized wind velocities when l_B is chosen according to Eq. 36. For $V_w = 12m/s$, values $v_w = 0.2, 0.1, 0.075$ and 0.06 correspond to $L_t = 0.367, 1.46, 2.6$ and 4 km. As shown in Panel (a), provided δ and l_B follow Eq. 36, kite ceiling is not affected significantly by the bridle. However, stable flight required a thorough choice of the bridle dimensions. A value $l_B = 3m$, giving $\delta \approx 83°$, provides stable flight for a wide range of tether lengths.

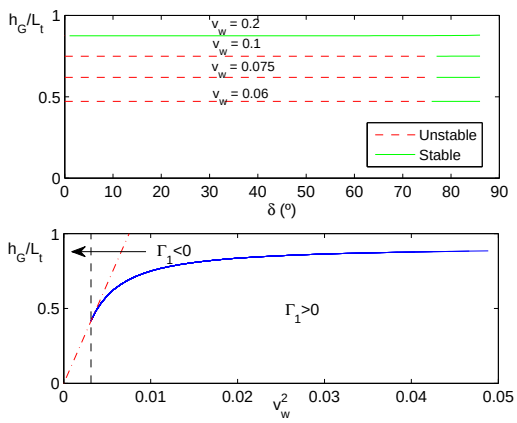

FIG. 8: Normalized kite altitude versus bridle angle δ.

The solid blue line in panel (b) of Fig. 8 shows the normalized altitude versus the square of the normalized wind velocity for $\delta = 83°$. The tether is above the ground ($\Gamma_1 > 0$) if $v_w^2 > 0.003$. Therefore, solutions from the dashed line to the left are not physical. This plot also shows that the ceiling, i.e. the maximum altitude, is reached when the tether is tangent to the ground. From $v_w = V_w/\sqrt{gL_t}$ one finds $h_G/L_t = \left(gh_G/V_w^2\right) \times v_w^2$. Therefore, for a given wind velocity V_w, the maximum altitude is reached when the slope of the curve h_G/L_t versus v_w^2 is maximum. As highlighted by the red dash-dot line in panel (b) this occurs close to the threshold that makes $\Gamma_1 = 0$.

Panel (a) in Fig. 9 shows the tether equilibrium position for three different tether lengths and the values of Table I, except $L_B = 3m$, $V_w = 12m/s$, and δ given by Eq. 36. For $L_t = 1.5$, 3 and 4.5 km kite altitudes are about 1.1, 1.7, and 1.9km. Clearly, the kite altitude increases with the tether length. However, the tether tension component along $\boldsymbol{k}_E$ at $s = 0$ (the ground attachment point) is reduced [see panel (b) 9]. It vanishes, i.e. the tether is tangent to the ground at $s = 0$ for $L_t \approx 4.7km$. This tether length, with a weight of $316N$, yields a ceiling of $h = 1950m$.

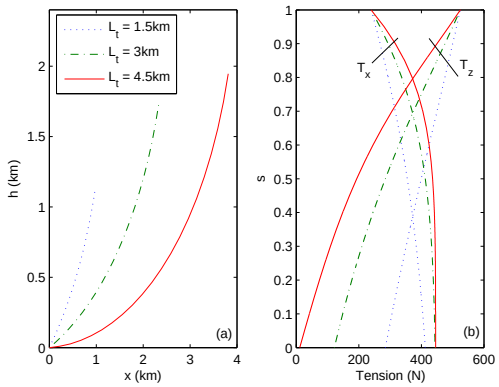

FIG. 9: Tether position (left) and tension versus arc-length (right).

VI. DISCUSSION

The use of models with disparate degrees of complexity and computational cost applied to a particular problem, i.e the stability of the kite equilibrium, allowed to clarify several aspects. The artificial constraint on the kite pitch angle $\theta = \pi/2 - \Gamma$ is qualitatively correct for kite equilibrium analysis because higher elevation angle of the tether are linked to smaller kite pitch angle [see panel (a) in Fig. 3]. However, such a constraint yields erroneous quantitative result on the minimum wind velocity for steady flight and its equilibrium (see panels (b) in Figs. 2 and 3). For this reason, we conclude that the elegant model

presented in Ref. [9] may be used only for academic and teaching purposes.

Among tether inertial effects and aerodynamic forces, the latter seems to be more critical in the stability analysis of kite equilibrium. All the results of this work indicates that accurate kite simulators should include the aerodynamic drag of the tether. Otherwise, the stability of the kite-tether equilibrium is undervalued (see panels (a) and (b) in Fig. 4). However, the models of this work probably underestimate kite stability because, except the damping term $f_t\dot{\epsilon}$ in Eq. 30 of the elastic tether model, structural damping has been totally ignored. Such effect can be incorporated easily to the bar-models by just adding ideal damper at the joints (terms proportional to $\sim \dot{\Gamma}_i$ in the equations of motion). We also checked that adding a term proportional to $C_{mq}\dot{\theta}$ ($C_{mq} < 0$) in the aerodynamic moment of the kite (Eq. 3) improves considerably the longitudinal stability of the kite.

A trade-off between reliability and computational cost indicates that the inelastic, but flexible, N-bar model is the most advantageous choice. One-bar models do not provide reliable results, except for short tethers with high tensions. They seem to be appropriate for preliminary designs. On the opposite side, the computational cost of the elastic tether model is very high because (i) the integrals in Eq. C14 have to be done numerically and (ii) since the model includes the fast longitudinal oscillations of the tether, the system is stiff. The N-bar model is free of these issues and also avoids the computation of the tension during the numerical integration of the equations. This later feature also distinguishes our N-bar model from Minakov theory.

Our bar-based models used the *minimal coordinate* approach, i.e. the constraint introduced by the tether was taken into account in the state vector, which contains the minimum number of variables that fully determine the state of the system. As a consequence, the tether tension (constraint force) has zero contribution in the generalized forces (Q_i) and it is eliminated from the equation of motion. An alternative is a *natural coordinate* approach. This method yields a nonlinear system of coupled algebraic and ordinary differential equations and typically needs artificial damping to stabilize the un-physical numerical drift of the constraints. However, although these comments may indicate that the minimal coordinate approach is the most advantageous choice, optimization schemes based on Newton like algorithm exhibited a better convergence with natural coordinates [23, 24]. In addition, the computation of the equation of motion with minimal coordinates also needs a considerable analytical effort that becomes very difficult as the complexity of the system is increased. Therefore, the choice of the best approach depends heavily on the complexity of the system and the use of the simulator (optimal control algorithms, stability analysis, periodic orbit determination, etc).

VII. CONCLUSIONS

This work presented a set of models that covers a wide spectrum of kite models; from a simple model with just 1-degree of freedom to a complex system including tether inertial, flexibility, and elasticity. Among all of them, the new N-bar model of this work has two important advantages: the resulting set of equations are not stiff and the tension force is naturally eliminated by using the Lagrangian formalism. The studies of the kite equilibrium stability and its ceiling highlighted the importance of the bridle design on kite performance.

The access to mathematical models of different complexities can benefit kite-tether system design applied to wind energy generation. This is typically an iterative process. It involves a preliminary phase driven by a list of requirements that is followed by optimization analysis and finally detailed simulations of the system. Simple and complex models with different computational costs are necessary at each phase. The comparison of the simulations allows to verify and validate the results before carrying out expensive experimental campaigns.

The application of the N-bar model to airborne wind energy generation with pumping maneuver requires two modifications of the code: fully three-dimensional dynamics of the kite-tether system and a time-dependent tether length. Both extensions are possible within the framework established in this work. The development of such a numerical tool would also benefit other areas like for instance the de-orbiting simulation of space debris by electrodynamic tethers.

APPENDIX A: EULER-LAGRANGE EQUATIONS FOR THE BAR-BASED TETHER MODEL

Substituting Eqs. 11-17 in Eq. 18 yields

$$\begin{aligned}\mathcal{L} = \frac{\sigma}{N^3}\sum_{i=1}^{N}\sum_{j=1}^{i}\left[\frac{p_j^2\dot{\Gamma}_j^2}{2} + \sum_{\substack{m=\\ j+1}}^{i} p_m\dot{\Gamma}_j\dot{\Gamma}_m\cos\left(\Gamma_j-\Gamma_m\right)\right] + \\ \frac{1}{N^2}\sum_{j=1}^{N}\left[\frac{\dot{\Gamma}_j^2}{2} - Nl_B\dot{\theta}\dot{\Gamma}_j\cos\gamma_j + \sum_{\substack{m=\\ j+1}}^{N}\dot{\Gamma}_j\dot{\Gamma}_m\cos\left(\Gamma_j-\Gamma_m\right)\right] \\ +\frac{1}{2}\left(l_B^2+i_k\right)\dot{\theta}^2 + \frac{\sigma}{2}\sum_{i=1}^{N} i_e\dot{\Gamma}_i^2 \\ -\frac{1}{N}\sum_{j=1}^{N}\sin\Gamma_j - l_B\sin\left(\delta-\theta\right) - \frac{\sigma}{N^2}\sum_{i=1}^{N}\sum_{j=1}^{i} p_j\sin\Gamma_j\end{aligned} \tag{A1}$$

with

$$\gamma_j \equiv \delta - \theta - \Gamma_j \tag{A2}$$

After inserting Eq. A1 in Eq. 1 and carrying out some cumbersome operations, one finds the equations of motion of the tether-kite system

$$\left[1+\frac{\sigma}{N}\left(\frac{1}{12}+\sum_{j=i}^{N}p_j^2\right)\right]\ddot{\Gamma}_i + \sum_{\substack{j=1\\ j\neq i}}^{N} A_{ij}\left[\ddot{\Gamma}_j\cos\left(\Gamma_i-\Gamma_j\right)+\dot{\Gamma}_j^2\sin\left(\Gamma_i-\Gamma_j\right)\right] - l_B N\left[\ddot{\theta}\cos\gamma_i+\dot{\theta}^2\sin\gamma_i\right]+B_i\cos\Gamma_i-N^2Q_{\Gamma_i}=0 \tag{A3}$$

$$\left(i_k+l_B^2\right)\ddot{\theta}-\frac{l_B}{N}\sum_{j=1}^{N}\left[\ddot{\Gamma}_j\cos\gamma_j+\dot{\Gamma}_j^2\sin\gamma_j\right] -l_B\cos\left(\delta-\theta\right)-Q_\theta=0 \tag{A4}$$

with

$$A_{ij}=\begin{cases}1+\frac{\sigma}{N}\left(N-j+1/2\right) & i<j\\ 1+\frac{\sigma}{N}\left(N-i+1/2\right) & i>j\end{cases} \tag{A5}$$

and

$$B_i=N+\sigma\sum_{j=i}^{N}p_j \tag{A6}$$

The generalized forces in Eqs. A3 and A4 are given by

$$Q_{\Gamma_i}=\frac{1}{N}\left(\sin\Gamma_i\boldsymbol{i}_E-\cos\Gamma_i\boldsymbol{k}_E\right)\cdot\left(\boldsymbol{f}_{Ak}+\frac{1}{2}\boldsymbol{f}_{At}^i+\sum_{j=i+1}^{N}\boldsymbol{f}_{At}^j\right) \tag{A7}$$

$$Q_\theta=\boldsymbol{m}_{Ak}\cdot\boldsymbol{j}_E-l\left[\sin\left(\delta-\theta\right)\boldsymbol{i}_E-\cos\left(\delta-\theta\right)\boldsymbol{k}_E\right]\cdot\boldsymbol{f}_{Ak} \tag{A8}$$

APPENDIX B: BAR-BASED MODEL USING CLASSICAL MECHANICS

This section computes the equations of motion of the kite-tether system using classical mechanics. The purpose is twofold. In first place, these equations can be used to compute the tether tension by post-processing the results obtained from Sys. A3-A4. In second place, the comparison of numerical integrations of the Lagrangian and the classical models was used as a test to verify the correct implementation of both codes.

The equations of motion of the bar i are (see Fig. 1)

$$\frac{\sigma}{N}a_{ix}=t_x^i-t_x^{i+1}+f_{Atx}^i \tag{B1}$$

$$\frac{\sigma}{N}a_{iz}=t_z^i-t_z^{i+1}+\frac{\sigma}{N}+f_{Atz}^i \tag{B2}$$

$$\frac{\sigma}{6N^2}\ddot{\Gamma}_i=\left(t_z^i+t_z^{i+1}\right)\cos\Gamma_i-\left(t_x^i+t_x^{i+1}\right)\sin\Gamma_i \tag{B3}$$

where we used the subscripts x and z to denote the vector components in the Earth frame. The acceleration of the bar is found by taking the derivative of Eq. 11, that yields

$$\boldsymbol{a}_i=\frac{1}{N}\sum_{j=1}^{i}p_j\left[\left(\dot{\Gamma}_j^2\cos\Gamma_j+\ddot{\Gamma}_j\sin\Gamma_j\right)\boldsymbol{i}_E +\left(\dot{\Gamma}_j^2\sin\Gamma_j-\ddot{\Gamma}_j\cos\Gamma_j\right)\boldsymbol{k}_E\right] \tag{B4}$$

Similarly, the equations of motion of the kite are

$$a_{kx}=t_x^{N+1}+f_{Ax} \tag{B5}$$

$$a_{kz}=t_z^{N+1}+f_{Az}+1 \tag{B6}$$

$$i_k\ddot{\theta}=m_{Ay}+l_B\left[t_x^{N+1}\sin\left(\delta-\theta\right)-t_z^{N+1}\cos\left(\delta-\theta\right)\right] \tag{B7}$$

with $\boldsymbol{t}^{N+1}$ is minus the tether tension at the attachment point Q. The kite acceleration, found by taking the derivative of Eq. 17, reads

$$\boldsymbol{a}_k=\frac{1}{N}\sum_{j=1}^{N}\left[\left(\dot{\Gamma}_j^2\cos\Gamma_j+\ddot{\Gamma}_j\sin\Gamma_j\right)\boldsymbol{i}_E +\left(\dot{\Gamma}_j^2\sin\Gamma_j-\ddot{\Gamma}_j\cos\Gamma_j\right)\boldsymbol{k}_E\right] +l_B\left[\dot{\theta}^2\cos\left(\delta-\theta\right)-\ddot{\theta}\sin\left(\delta-\theta\right)\right]\boldsymbol{i}_E +l_B\left[\dot{\theta}^2\sin\left(\delta-\theta\right)+\ddot{\theta}\cos\left(\delta-\theta\right)\right]\boldsymbol{k}_E \tag{B8}$$

Since there are three equations like B1-B3 for each bar of the model and three equations governing the kite (B5-B7), one has $3\left(N+1\right)$. The unknowns are the angles Γ_i with i=1...N, the kite pitch angle θ and the tether tension components T_x^i and T_z^i with $i=1,N+1$. Therefore, the system has $3\left(N+1\right)$ unknowns. As compared with the Lagrangian Equations (A3-A4), we observe that the classical formulation has two major drawbacks. In first place, the size of the system is larger ($3\left(N+1\right)$ instead of $N+1$). In second place, the numerical integration of Sys. B1-B3 and B5-B7 needs at each time step a Newton method to determine the tether tension. This makes the model based on classical mechanics more expensive from a computational point of view.

If the evolution of the kite-tether system, i.e. the state vector $\boldsymbol{x}_s(\tau)$ and its two first derivatives $\dot{\boldsymbol{x}}_s(\tau)$ and $\ddot{\boldsymbol{x}}_s(\tau)$, were found by integrating Eqs. A3-A4 numerically, one can use the classical equations to find the tension at the bar joints. At each time, the acceleration of the bars and the kite are computed by using Eqs. B4 and B8. Similarly, the aerodynamic forces acting on the the bars and the kite can be evaluated with $\boldsymbol{x}_s(\tau)$ and $\dot{\boldsymbol{x}}_s(\tau)$. These results are then used in Eqs. B5 and B6 to find t_x^{N+1} and t_z^{N+1}. The recursively evaluation of Eqs. B1 and B2 with $i=N,N-2,...2,1$ provides the tension values at every joint.

APPENDIX C: ELASTIC TETHER-KITE MODEL

The position and velocity vectors of the center of mass of the kite are

$$\begin{aligned}\boldsymbol{r}_k =& -\left[r\cos\left(\Gamma+\theta\right)+l_B\cos\delta\right]\boldsymbol{i}_B \\ &-\left[r\sin\left(\Gamma+\theta\right)+l_B\sin\delta\right]\boldsymbol{k}_B\end{aligned} \tag{C1}$$

$$\begin{aligned}\boldsymbol{v}_k =& \left[r\dot{\Gamma}\sin\left(\Gamma+\theta\right)-\dot{r}\cos\left(\Gamma+\theta\right)-l_B\dot{\theta}\sin\delta\right]\boldsymbol{i}_B \\ &-\left[r\dot{\Gamma}\cos\left(\Gamma+\theta\right)+\dot{r}\sin\left(\Gamma+\theta\right)-l_B\dot{\theta}\cos\delta\right]\boldsymbol{k}_B\end{aligned} \tag{C2}$$

and the angular velocity $\boldsymbol{\omega}_k = \dot{\theta}\boldsymbol{j}_E$. The Lagrangian of the kite reads

$$\begin{aligned}\mathcal{L}_k =& \frac{1}{2}\left[r^2\dot{\Gamma}^2+\dot{r}^2+\left(l_B^2+i_k\right)\dot{\theta}^2\right]+l_B\dot{\theta}\left(\dot{r}\sin\gamma-r\dot{\Gamma}\cos\gamma\right) \\ &-r\sin\Gamma+l_B\sin\left(\theta-\delta\right)\end{aligned} \tag{C3}$$

with γ given by Eq. A2. The computation of the generalized forces in Eq. 18 should now include the normalized tension $\boldsymbol{t}_Q(\tau) = -\boldsymbol{t}(s=1,\tau)$ applied at the point Q of the kite bridle. They reads

$$Q_\Gamma = \left(\boldsymbol{f}_{Ak}+\boldsymbol{t}_Q\right)\cdot\frac{\partial\boldsymbol{v}_k}{\partial\dot{\Gamma}} \tag{C4}$$

$$Q_\theta = \left(\boldsymbol{f}_{Ak}+\boldsymbol{t}_Q\right)\cdot\frac{\partial\boldsymbol{v}_k}{\partial\dot{\theta}}+\left(\boldsymbol{m}_{Ak}+\overline{GQ}\times\boldsymbol{t}_Q\right)\cdot\frac{\partial\boldsymbol{\omega}_k}{\partial\dot{\theta}_i} \tag{C5}$$

$$Q_r = \left(\boldsymbol{f}_{Ak}+\boldsymbol{t}_Q\right)\cdot\frac{\partial\boldsymbol{v}_k}{\partial\dot{r}} \tag{C6}$$

The equations of motion of the kite are

$$\begin{pmatrix} r & -l\cos\gamma & 0 \\ -r\cos\gamma & \frac{l^2+i_k}{l} & -\sin\gamma \\ 0 & -l\sin\gamma & 1 \end{pmatrix}\begin{pmatrix}\ddot{\Gamma}\\ \ddot{\theta}\\ \ddot{r}\end{pmatrix} = \begin{pmatrix} Q_\Gamma - l\dot{\theta}^2\sin\gamma-\cos\Gamma-2\dot{r}\dot{\Gamma} \\ Q_\theta - r\dot{\Gamma}^2\sin\gamma+\cos\left(\theta-\delta\right)+2\dot{r}\dot{\Gamma}\cos\gamma \\ Q_r + l\dot{\theta}^2\cos\gamma+r\dot{\Gamma}^2-\sin\Gamma \end{pmatrix} \tag{C7}$$

Regarding the tether, Eq. 29 was discretized following a finite-element method for space tethers [15]. The tether is divided into N uniform elements of length $l_e = 1/N$ and we introduced $N+1$ nodes according to $\boldsymbol{r}_j(\tau) \equiv \boldsymbol{r}(\tau, s_j)$ with $s_j = (j-1)l_e$ and $j = 1, 2, ...N+1$. The local nodal basis functions for a single element j are the cubic Hermite polynomials

$$N_1^j = 1-3\xi_j^2+2\xi_j^3 \tag{C8}$$

$$N_2^j = \xi_j-2\xi^2+\xi_j^3 \tag{C9}$$

$$N_3^j = 3\xi_j^2-2\xi_j^3 \tag{C10}$$

$$N_4^j = -\xi_j^2+\xi_j^3 \tag{C11}$$

with the element natural coordinate $\xi_j = (s-s_j)/l_e$ and $\xi_j \in [0\ 1]$. This choice gives continuity for the displacement and the slope at the nodes. The vector position over the element j is expanded as

$$\boldsymbol{r}^j(\tau,\xi) = \sum_{k=0}^{1}\boldsymbol{r}_{j+k}(\tau)N_{2k+1}^j(\xi)+\frac{d\boldsymbol{r}_{j+k}(\tau)}{d\xi}N_{2k+2}^j(\xi) \tag{C12}$$

Applying principles of finite elements, local nodal basis functions N_i^j are used to form the global nodal basis functions ϕ_j and write the position vector of the tether as

$$\boldsymbol{r}_t(\tau,s) = \sum_{j=1}^{2(N+1)}\boldsymbol{C}_j(\tau)\phi_j(s) \tag{C13}$$

where, due to the properties of the Hermite polynomials, C_j is a node position when j is odd and a slope when j is even.

The weak form of Eq. 29 is found by multiplying it by the functions $\phi_i(s)$ and integrating between $0 \le s \le 1$

$$M_{ij}\ddot{C}_j = b_i\boldsymbol{k}_E+\phi_i\boldsymbol{t}\,|_0^1+\int_0^1\left[\chi\left(\boldsymbol{v}_A\cdot\boldsymbol{u}_\perp\right)^2\phi_i\boldsymbol{u}_\perp-\phi_i'\boldsymbol{t}\right]ds \tag{C14}$$

where

$$M_{ij} = \sigma\int_0^1\phi_i(s)\phi_j(s)ds, \qquad b_i = \sigma\int_0^1\phi_i ds \tag{C15}$$

The boundary conditions 31-34, which gives $\boldsymbol{C}_1 = \dot{\boldsymbol{C}}_1 = 0$, $\boldsymbol{C}_{2N+1} = \boldsymbol{r}_Q$ and $\dot{\boldsymbol{C}}_{2N+1} = \boldsymbol{v}_Q$, are applied to Sys. C14 for all time. The state vector for the kite-tether system is

$$\begin{aligned}\boldsymbol{u}(\tau) = [&\Gamma\ \theta\ r\ \boldsymbol{C}_2\ \boldsymbol{C}_3\ \ldots\boldsymbol{C}_{2N}\ \boldsymbol{C}_{2(N+1)} \\ &\dot{\Gamma}\ \dot{\theta}\ \dot{r}\ \dot{\boldsymbol{C}}_2\ \dot{\boldsymbol{C}}_3\ \ldots\dot{\boldsymbol{C}}_{2N}\ \dot{C}_{2(N+1)}]\end{aligned} \tag{C16}$$

and it is governed by the ordinary differential equations C7 and Eqs C14 (after applying the boundary conditions).

The implementation of the elastic tether model was validated by comparing the code results with the catenary solution of Eq. 29 for $\chi = 0$, which is given by

$$x(s) = D_1\left\{s-\frac{1}{\alpha_0}\left[\sinh^{-1}\left(\zeta(s)\right)-\sinh^{-1}\left(\zeta(0)\right)\right]\right\} \tag{C17}$$

$$z(s) = D_2 s-\frac{1}{2}\alpha_0 s^2-\frac{D_1}{\alpha_0}\left[\sqrt{1+\zeta(s)^2}-\sqrt{1+\zeta^2(0)}\right] \tag{C18}$$

with $\alpha_0 \equiv \sigma/\nu$, $\zeta(s) = (D_2-\alpha_0 s)/D_1$ and D_1 and D_2 two constants that are found by imposing $x(s=1) = -r\cos\Gamma$ and $z(s=1) = -r\sin\Gamma$.

ACKNOWLEDGMENTS

This work was supported by Fundación BBVA under the *Convocatoria 2015 de Ayudas BBVA a*

Investigadores y Creadores Culturales, Grant No. IN[15]_TIC_ING_0313. G.S.A was supported by the Ministerio de Economía y Competitividad of Spain (Grant No RYC-2014-15357)

REFERENCES

[1] Loyd, M. L., "Crosswind Kite Power," *J. Energy*, Vol. 4, No. 3, 1980, pp. 24–30.
doi: 10.2514/3.48021

[2] Williams, P., Lansdorp, B., and Ockels, W., "Optimal crosswind towing and power generation with tethered kites," *Journal of Guidance, Control and Dynamics*, Vol. 31, No. 1, 2008, pp. 81–93.
doi: 10.2514/1.30089

[3] Schmehl, R., "Kiting for wind power," *Wind Systems*, Vol. 27, No. 7, 2012, pp. 36–43.

[4] Fagiano, L. and Milanese, M., "Airborne Wind Energy: An overview," *2012 American Control Conference (ACC)*, June 2012, pp. 3132–3143.
doi: 10.1109/ACC.2012.6314801

[5] Bryson, M., Johnson-Roberson, M., Murphy, R. J., and Bongiorno, D., "Kite Aerial Photography for Low-Cost, Ultra-high Spatial Resolution Multi-Spectral Mapping of Intertidal Landscapes," *PLoS ONE*, Vol. 8, No. 9, 2013, pp. e73550.

[6] Groot, S. D., Breukels, J., Schmehl, R., and Ockels, W., "Modelling Kite Flight Dynamics Using a Multibody Reduction Approach," *Journal of Guidance, Control, and Dynamics*, Vol. 34, No. 6, 2011, pp. 1671–1682.
doi: 10.2514/1.52686

[7] Fechner, U., van der Vlugt, R., Schreuder, E., and Schmehl, R., "Dynamic model of a pumping kite power system," *Renewable Energy*, Vol. 83, 2015, pp. 705 – 716.
doi: 10.1016/j.renene.2015.04.028

[8] Bosch, A., Schmehl, R., Tiso, P., and Rixen, D., "Dynamic Nonlinear Aeroelastic Model of a Kite for Power Generation," *Journal of Guidance, Control, and Dynamics*, Vol. 37, No. 5, 2013, pp. 1426 – 1436.
doi: 10.2514/1.G000545

[9] Adomaitis, R. A., "Kites and bifurcation theory," *SIAM Review*, Vol. 31, No. 3, 1989, pp. 478.

[10] Sánchez-Arriaga, G., "Dynamics and control of single line kites," *The Aeronautical Journal*, Vol. 110, No. 1111, 2006, pp. 615–621.
doi: 10.1017/S0001924000001470

[11] Sánchez-Arriaga, G., Garcia-Villalba, M., and Schmehl, R., "A two-line kite dynamic model for airborne wind energy generation," *(submited to Applied Mathematical Modelling)*.

[12] Williams, P., Lansdorp, B., and Ockels, W., "Nonlinear control and estimation of a tethered kite in changing wind conditions," *Journal of Guidance, Control and Dynamics*, Vol. 31, No. 3, 2008, pp. 793–799.
doi: 10.2514/1.31604

[13] Zanon, M., Gros, S., and Andersson, J., "Airborne Wind Energy Based on Dual Airfoils ," *IEEE Transactions on Control Systems Technology*, Vol. 21, No. 4, 2013, pp. 1215–1222.
doi: 10.1109/TCST.2013.2257781

[14] Gohl, F. and Luchsinger, R. H., "Simulation Based Wing Design for Kite Power," *Airborne Wind Energy*, edited by U. Ahrens, M. Diehl, and R. Schmehl, chap. 18, Springer-Verlag Berlin Heidelberg, 2013, pp. 325–338.

[15] Ellis, J. and Hall, C. D., "Model Development and Code Verification for Simulation of Electrodynamic Tether System," *Journal of Guidance, Control, and Dynamics*, Vol. 32, No. 6, 2009, pp. 1713–1722.
doi: 10.2514/1.44638

[16] Beletskii, V. and Levin, E., *Dynamics of space tether systems*, edited by A. A. Society, Advances in astronautical sciences, chap. 2, Published for the American Astronautical Society by Univelt, Inc., 1993, pp. 61-114

[17] Peláez, J., López-Rebollal, O., Lorenzini, E., and Cosmos, M. L., "Two-Bar Model for the Dynamics and Stability of Electrodynamic Tethers," *Journal of Guidance, Control, and Dynamics*, Vol. 25, No. 6, 2002, pp. 1125–1135.
doi: 10.2514/2.4992

[18] Puig-Suari, J., Logunski, J. M., Tragesser, S. G.,, "Aerocapture with a flexible tether," *Journal of Guidance, Control, and Dynamics*, Vol. 18, No. 6, 1995, pp. 1305–1312.
doi: 10.2514/3.21546

[19] Biswell, B., Logunski, J. M., Puig-Suari, J., Tragesser, S. G.,, "Three-Dimensional Hinged-Rod Model for Elastic Aerobraking Tethers," *Journal of Guidance, Control, and Dynamics*, Vol. 21, No. 2, 1998, pp. 286–295.
doi: 10.2514/2.4234

[20] Terink, E., Breukels, J., Schmehl, R., and Ockels, W., "Flight Dynamics and Stability of a Tethered Inflatable Kiteplane," *AIAA Journal of Aircraft*, Vol. 48, No. 2, 2012, pp. 503–513.
doi: 10.2514/1.C031108

[21] Salord Losantos, L. and Sánchez-Arriaga, G., "Flight Dynamics and Stability of Kites in Steady and Unsteady Wind Conditions," *Journal of Aircraft*, Vol. 52, No. 2, 2015, pp. 660–666.
doi: 10.2514/1.C032825

[22] Alonso-Pardo, J. and Sanchez-Arriaga, G., "Kite Model with Bridle Control for Wind-Power Generation," *Journal of Aircraft*, Vol. 52, No. 3, 2015, pp. 917–923.
doi: 10.2514/1.C033283

[23] Gros, S. and Diehl, M., "Modeling of Airborne Wind Energy Systems in Natural Coordinates," *Airborne Wind Energy*, edited by U. Ahrens, M. Diehl, and R. Schmehl, chap. 10, Springer-Verlag Berlin Heidelberg, 2013, pp. 181–203.

[24] Horn, G., Gros, S. and Diehl, M., "Numerical Trajectory Optimization for Airborne Wind Energy Systems Described by High Fidelity Aircraft Models," *Airborne Wind Energy*, edited by U. Ahrens, M. Diehl, and R. Schmehl, chap. 11, Springer-Verlag Berlin Heidelberg, 2013, pp. 205–218.

[25] Hobbs, S. E., *A Quantitative study of kite performance in natural wind with application to kite anemometry*, Ph.D. thesis, Cranfield Institute of Technology, Indiana, 1986.

[26] Argatov, I., Rautakorpi, P., and Silvennoinen, R., "Apparent wind load effects on the tether of a kite power generator," *Journal of Wind Engineering and Industrial Aerodynamics*, Vol. 99, No. 10, 2011, pp. 1079–1088, Contribution: organisation=mat,FACT1=1.
doi: http://dx.doi.org/10.1016/j.jweia.2011.07.010

[27] Hoerner, S., *Fluid-dynamic drag: practical information on aerodynamic drag and hydrodynamic resistance*, Hoerner Fluid Dynamics, 1965.

[28] Varma, S. K. and Goela, J. S., "Effect of wind loading on the design of a kite tether," *Journal of Energy*, Vol. 6, No. 5, 1982, pp. 342–343.
doi: 10.2514/3.48051

[29] Macdonald, J. and Larose, G., "A unified approach to aerodynamic damping and drag/lift instabilities, and its application to dry inclined cable galloping," *Journal of Fluids and Structures*, Vol. 22, No. 2, 2006, pp. 229 – 252.
doi: http://dx.doi.org/10.1016/j.jfluidstructs.2005.10.002.

[30] Sternberg, J. and Goit, J., and Gros, S., and Meyers, J., and Diehl, M., "Robust and Stable Periodic Flight of Power Generating Kite Systems in a Turbulent Wind Flow Field," *IFAC Proceedings Volumes*, Vol. 45, No. 25, 2012, pp. 140 – 145.
doi: 10.3182/20120913-4-IT-4027.00009